Multi-Oriented Windowed Harmonic Phase Reconstruction for Robust Cardiac Strain Imaging

Lucilio Cordero-Grande*,a,b, Javier Royuela-del-Val[a], Santiago Sanz-Estébanez[a], Marcos Martín-Fernández[a], Carlos Alberola-López[a]

[a]*Laboratorio de Procesado de Imagen, Department of Teoría de la Señal y Comunicaciones e Ingeniería Telemática, ETSIT, Universidad de Valladolid, Campus Miguel Delibes s.n., 40011, Valladolid, Spain. Phone: +34 983 423660 ext. 5590.*
[b]*Centre for the Developing Brain and Department of Biomedical Engineering, Division of Imaging Sciences and Biomedical Engineering, King's College London, St Thomas' Hospital, SE1 7EH, London, UK. Phone: +44 020 7188 7118 ext. 53623.*

Abstract

The purpose of this work is to develop a method for direct estimation of the cardiac strain tensor by extending the harmonic phase reconstruction on tagged magnetic resonance images to obtain more precise and robust measurements. The extension relies on the reconstruction of the local phase of the image by means of the windowed Fourier transform and the acquisition of an overdetermined set of stripe orientations in order to avoid the phase interferences from structures outside the myocardium and the instabilities arising from the application of a gradient operator. Results have shown that increasing the number of acquired orientations provides a significant improvement in the reproducibility of the strain measurements and that the acquisition of an extended set of orientations also improves the reproducibility when compared with acquiring repeated samples from a smaller set of orientations. Additionally, biases in local phase estimation when using the original harmonic phase formulation are greatly diminished by the one here proposed. The ideas here presented allow the design of new methods for motion sensitive magnetic resonance imaging, which could simultaneously improve the resolution, robustness and accuracy of motion estimates.

Key words: Tagged Magnetic Resonance Imaging, Harmonic Phase Reconstruction, Artifacts, Strain Tensor, Windowed Fourier Transform

1. Introduction

Magnetic Resonance (MR) tagging allows to track material points through time. This is of special relevance, for instance, in the analysis of myocardial local motion, whose anomalies are directly related with impaired cardiac function. Hence, local functional indicators extracted from this analysis such as the strain tensor may provide a higher predictive value than global cardiac imaging parameters such as the ejection fraction (Axel et al., 2005; Simpson et al., 2013). The basis of MR tagging consists in the generation of a set of saturated magnetization planes which may be subsequently tracked throughout the cardiac cycle so as to estimate the motion of material points (Shehata et al., 2009; Ibrahim, 2011; Jeung et al., 2012). Usually, these planes are arranged in a parallel setting in such a way that the imaged magnetization is modulated by a given wave vector.

Regarding the analysis of MR tagging, an important family of methods are based on extracting the phase of the complex image obtained by filtering the isolated peaks of the spectrum that correspond to the magnetization modulation. Hence, this class of methods performs motion estimation by phase-based optical flow, in which the constant pixel brightness assumption is replaced by the potentially more reliable constant pixel phase assumption. The seminal work by Osman et al. (2000) shows that this HARmonic Phase (HARP) methodology not only permits to reconstruct small displacements[1] but also to reconstruct the deformation gradient tensor without imposing any condition on the deformation field. Furthermore, this technique is generally faster than intensity-based ones and, in addition, dense measurements can be recovered. Despite its potential, without a proper reconstruction scheme, it is prone to be corrupted by intravoxel phase dispersion, noise, and spectral interferences (especially at the endo- and epicardial boundaries), which are further accentuated in the estimation of the deformation gradient tensor, as it involves the application of a gradient operator on the reconstructed phases. Not coincidentally, a recent study by Swoboda et al. (2014) has

---

*Corresponding author

Email addresses: `lucilio.cordero_grande@kcl.ac.uk` (Lucilio Cordero-Grande), `jroyval@lpi.tel.uva.es` (Javier Royuela-del-Val), `ssanest@lpi.tel.uva.es` (Santiago Sanz-Estébanez), `marcma@tel.uva.es` (Marcos Martín-Fernández), `caralb@tel.uva.es` (Carlos Alberola-López)

[1]Although, for accurately doing so, motion tracking methods should be adapted to the information provided by HARP.

reported a somewhat poor interstudy and intrastudy reproducibility of strain measurements using the HARP method.

A comprehensive description of HARP reconstruction that pays attention to its dynamic range, resolution, noise properties, and characteristic artifacts is provided in Parthasarathy (2006). First, following Osman et al. (2000), a communications theory description of tagged images is developed which establishes that these images can be interpreted as the spatial analogue of an AM-FM signal so that the tissue strain would be equivalent to the instantaneous frequency of the signal. The author claims that HARP reconstruction is a way to obtain the instantaneous (i.e. local) phase of the signal on the basis of the monocomponent assumption, which states that the signal can be described by a single spectral component that modulates a narrow range of Fourier harmonics that vary as a function of time. With this interpretation in mind, HARP can be understood as a spatial phase demodulation technique and therefore part of the vast literature on temporal phase demodulation could be adapted for motion estimation. In Cordero-Grande et al. (2011), we proposed one technique to demodulate the local phase where we showed the relevance of balancing the spatio-spectral concentration of the HARP filters (trying to follow the spatial variation of the orientation and spacing of the tag pattern) by using the Windowed Fourier Transform (WFT). This Windowed HARP (WHARP) technique turned out to be effective in improving the accuracy in the reconstruction of the local phase. Subsequently, the method has been refined in Fu et al. (2013) by estimating the widths of the WFT on the basis of the instantaneous spatial frequencies as given by a Gabor Wavelet Transform analysis.

On the other hand, also in Parthasarathy (2006), a characterization of the main artifacts observed in HARP reconstructed images is carried out. In the circumferential strain case, the author describes the causes involved in the presence of a so-called zebra artifact as well as the reason why the radial strain estimation using the conventional HARP method is usually highly inaccurate —limitations in estimating radial strain have also been reported for other methods (Tobon-Gomez et al., 2013)—. However, the proposed strategy for the improvement of strain estimation is based on postprocessing the strain maps in order to diminish the influence of corrupted estimations —see also Abd-Elmoniem et al. (2006)—. Here we suggest a completely different methodology for improving the strain reconstruction using the HARP method which resembles previous contributions such as using Complementary SPAtial Modulation of Magnetization (Kuijer et al., 2001) (CSPAMM)

or TruHARP (Agarwal et al., 2010) in that it tries to resolve the corrupted areas of the estimated tensor using additional data rather than postprocessing. However, instead of varying the phase of the modulation function to remove spectral peaks interferences, we propose a complementary approach that consists in the acquisition of an overdetermined set of stripe orientations in order to get rid of the orientation dependent phase interferences. This idea has been usually applied in diffusion tensor imaging acquisitions (Papadakis et al., 1999; Jones et al., 1999), where an overdetermined set of gradient orientations have proven to be beneficial in order to diminish the noise in the reconstruction of the diffusion tensor (and mandatory in order to obtain non-Gaussian representations of the diffusion). Preliminary versions of this work have been presented in the past (Cordero-Grande and Alberola-López, 2012; Cordero-Grande et al., 2014) and some other related techniques have been suggested recently (Bruurmijn et al., 2013); here, we give the full details of the equations involved and provide experimental evidence about the improvement in the accuracy and reproducibility of the strain estimates obtained by the proposed Multi-Oriented Windowed HARP (MOWHARP) method with respect to standard HARP.

In Section 2 we present the theory behind the MOWHARP method; the application of this methodology to real data is described in Section 3; main results regarding the reproducibility of measurements and implications of the experiments carried out are included in Section 4; insight into the practical application of the proposed methodology together with its main advantages and drawbacks are provided in Section 5; and conclusions are established in Section 6.

2. Theory

MR tagging is usually performed by SPAMM (Axel and Dougherty, 1989) or a variant of this technique. SPAMM is grounded on the ability of altering the magnetization of the tissue (within the limitations of relaxation times in MR) even in the presence of motion. The tagging procedure is based on the superposition of a spatial modulation over the applied gradients. To achieve this, a ψ_0 radiofrequency (RF) pulse must be applied, followed by P joint applications of a gradient and another pulse ψ_p. This process will generate a spatial modulation by P sinusoidal functions on the gradient direction. Thus, just after the application of a spatial modulation indexed by i and given by a wave vector $\mathbf{k}_i$, with $\mathbf{k}_i = k_i \mathbf{u}_i$, where k_i is the wave number of

the modulation (which depends on the amplitude of the applied gradient) and $\mathbf{u}_i$ is its orientation vector (which corresponds to the orientation of the applied gradient), the image equation is written

$$I_i(\mathbf{X}) = I^0(\mathbf{X}) \sum_{p=0}^{P} c_p \cos(2\pi p \mathbf{k}_i^T \mathbf{X}), \tag{1}$$

where $\mathbf{X}$ denotes the material coordinate, $I^0(\mathbf{X})$ corresponds to the anatomic image, P is the SPAMM order, and c_p is a set of amplitude terms that depend on the train of RF pulses applied. This modulation is translated into a convolution with a Dirac δ distribution in the spectral domain:

$$S_i(\mathbf{k}) = \sum_{p=0}^{P} \frac{c_p}{2} (S^0(\mathbf{k} + p\mathbf{k}_i) + S^0(\mathbf{k} - p\mathbf{k}_i)), \tag{2}$$

with S_i and S^0 being, respectively, the FTs of I_i and I^0. In high order SPAMM the sharpness of the magnetization profiles is controlled by choosing different amplitude terms.

The temporal evolution of a SPAMM image can be written as

$$I_i(\mathbf{x}, t) = I^0(\mathbf{X}(\mathbf{x}, t)) \sum_{p=0}^{P} c_p(\mathbf{X}(\mathbf{x}, t), t) \cos(2\pi p \mathbf{k}_i^T \mathbf{X}(\mathbf{x}, t)) \tag{3}$$

where $\mathbf{x}$ denotes the spatial coordinate, $\mathbf{X}(\mathbf{x}, t)$ denotes the material coordinate $\mathbf{X}$ corresponding to the spatial coordinate $\mathbf{x}$ at time t, and $c_p(\mathbf{X}, t)$ varies in t due to the T_1 relaxation of the tissue at $\mathbf{X}$. For the 1-1 SPAMM acquisition one has that $P = 1$ (Crum et al., 1998) and, assuming $\psi = \psi_0 = \psi_1$,

$$\begin{aligned} c_0(\mathbf{X}, t) &= 1 - \sin^2(\psi) e^{-\frac{t}{T_1(\mathbf{X})}} \\ c_1(\mathbf{X}, t) &= \sin^2(\psi) e^{-\frac{t}{T_1(\mathbf{X})}}. \end{aligned} \tag{4}$$

A commonly used value is $\psi = 45°$ in order to preserve the positivity of the image and maximize the tag contrast. Additionally, in 1-1 SPAMM, the wave number is inversely proportional to the wavelength or spacing of the stripes, $k_i = 1/\lambda_i$.

In this paper we focus on 2D MR HARP images, as 3D acquisitions are rarely used in clinical practice. As stated in Osman et al. (2000), 2D HARP

motion reconstruction using the SPAMM technique requires a minimum of 2 linearly independent wave vectors. Our proposal extends the aforementioned HARP methodology for the estimation of the deformation gradient tensor by allowing the application of a set of $I \geq 2$ wave vectors (with a minimum of 2 of them being linearly independent) and present the reconstruction equations in this case. The reconstruction is decomposed in the following steps:

- Calculation of the local phase of the image (Section 2.1). This step is based on the method presented in Cordero-Grande et al. (2011).

- Estimation of the material deformation gradient tensor (Section 2.2). This step is based on the method presented in Cordero-Grande and Alberola-López (2012) for synthetic data and preliminarily applied to real data in Cordero-Grande et al. (2014).

- Calculation of the Green-Lagrange strain tensor (Section 2.3). This step expresses the Green-Lagrange strain tensor in terms of the material deformation gradient tensor.

2.1. Local phase

Let $\mathbf{k}_i^T = k_i \mathbf{u}_i = k_i(u_i^1, u_i^2)$, with $1 \leq i \leq I$ be the set of acquired wave vectors. For a given cardiac phase, we denote the image corresponding to one of the acquired wave vectors as $I_i[\mathbf{n}]$, where $\mathbf{n} = [n^1, n^2]$, with $1 \leq n^j \leq N^j$ ($j = \{1, 2\}$), where N^j is the number of pixels along direction j. By periodically extending this image with period $\mathbf{N} = [N^1, N^2]$, we can define its 2D discrete WFT as:

$$S_i[\mathbf{m}, \mathbf{q}] = \frac{1}{Q^1 Q^2} \sum_{n^1, n^2 = -\infty}^{\infty} I_i[\mathbf{n}] w[\mathbf{n} - \mathbf{m}] e^{-j2\pi \sum_{j=1}^{2} \frac{q^j n^j}{Q^j}}, \qquad (5)$$

where $\mathbf{m} = [m^1, m^2]$ with $1 \leq m^j \leq N^j$, $\mathbf{q} = [q^1, q^2]$ with $1 \leq q^j \leq Q^j$, and w represents an analysis window of compact support whose size is $\mathbf{Q} = [Q^1, Q^2]$. This window is real, even, of unit norm, and monotonically decreasing for positive values of its argument. Hence, the discrete WFT is defined as a set of discrete FTs of the result of windowing an image throughout its support.

The WFT provides a representation of the image spectrum in the surroundings of each pixel of the original image, so HARP Band-Pass (BP)

filtering techniques can be directly applied on the spatially localized spectrum of the image. Then, for each pixel $\mathbf{m}$, we build a filter H_i parameterized spatially by $\boldsymbol{\lambda}$, $H_i^{\boldsymbol{\lambda}}[\mathbf{m}, \mathbf{q}] = H_i^{\boldsymbol{\lambda}[\mathbf{m}]}[\mathbf{q}]$ to filter the WFT:

$$\hat{S}_i[\mathbf{m}, \mathbf{q}] = H_i^{\boldsymbol{\lambda}}[\mathbf{m}, \mathbf{q}] S_i[\mathbf{m}, \mathbf{q}] \tag{6}$$

The WHARP image can be reconstructed in the spatial domain by using an Inverse discrete WFT (IWFT)

$$\hat{I}_i[\mathbf{n}] = \sum_{m^1, m^2=-\infty}^{\infty} \sum_{q^1=1}^{Q^1} \sum_{q^2=1}^{Q^2} \hat{S}_i[\mathbf{m}, \mathbf{q}] w[\mathbf{n} - \mathbf{m}] e^{j2\pi \sum_{j=1}^{2} \frac{q^j n^j}{Q^j}} \tag{7}$$

and extracting the phase:

$$\phi_i[\mathbf{n}] = \angle \hat{I}_i[\mathbf{n}]. \tag{8}$$

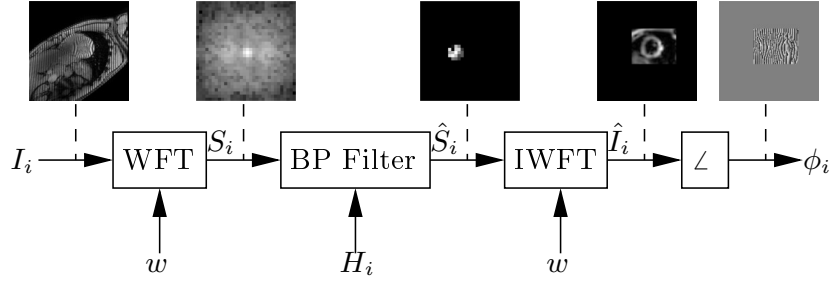This procedure for local phase estimation is sketched in Figure 1.

Figure 1: Flowchart of the local phase calculation. The analysis is performed in a region of interest surrounding the myocardium. For those steps in which a complex signal is generated, only the magnitude and logarithm of the magnitude (respectively for spatial and spectral signals) is represented.

2.2. Material deformation gradient tensor

We can arrange the set of wave vectors $\mathbf{k}_i^T$ in matrix form by:

$$\mathbf{K} = 2\pi \begin{pmatrix} \mathbf{k}_1^T \\ \mathbf{k}_2^T \\ \vdots \\ \mathbf{k}_I^T \end{pmatrix}, \tag{9}$$

so the linear independence condition implies that rank$(\mathbf{K}) = 2$. The spatial deformation gradient tensor

$$\mathbf{f}(\mathbf{x}) = \frac{\partial \mathbf{X}}{\partial \mathbf{x}^T}(\mathbf{x}) \tag{10}$$

is related with the gradient of the local phase $\phi_i(\mathbf{x})$ by (Osman et al., 2000):

$$2\pi \mathbf{k}_i^T \mathbf{f}(\mathbf{x}) = \frac{\partial^* \phi_i}{\partial \mathbf{x}^T}(\mathbf{x}) = \min\left\{ \frac{\partial \phi_i}{\partial \mathbf{x}^T}(\mathbf{x}), \frac{\partial \mathcal{W}(\phi_i + \pi)}{\partial \mathbf{x}^T}(\mathbf{x}) \right\}, \tag{11}$$

with $\mathcal{W}(\cdot)$ the wrapping operator, which maps its argument in the interval $[-\pi, \pi)$. The discretization of the gradient operator is achieved by first applying forward and backward finite differences both for the original phase and the π-shifted one, then taking the minimum as indicated in (11), and finally averaging them to construct the centered finite differences.

Rearranging the gradient of the phase images in matrix form:

$$\mathbf{Y}(\mathbf{x}) = \begin{pmatrix} \dfrac{\partial^* \phi_1}{\partial \mathbf{x}^T}(\mathbf{x}) \\[2ex] \dfrac{\partial^* \phi_2}{\partial \mathbf{x}^T}(\mathbf{x}) \\[2ex] \vdots \\[2ex] \dfrac{\partial^* \phi_I}{\partial \mathbf{x}^T}(\mathbf{x}) \end{pmatrix}, \tag{12}$$

one has (now in discrete form)

$$\mathbf{Y}[\mathbf{n}] = \mathbf{K}\mathbf{f}[\mathbf{n}]. \tag{13}$$

Alternatively, the material deformation gradient tensor $\mathbf{F}[\mathbf{n}] = \mathbf{f}^{-1}[\mathbf{n}]$ can be described by:

$$\mathbf{K} = \mathbf{Y}[\mathbf{n}]\mathbf{F}[\mathbf{n}]. \tag{14}$$

In order to estimate $\mathbf{F}[\mathbf{n}]$, one could resort to the Least Squares (LS) method, so:

$$\mathbf{F}[\mathbf{n}] = (\mathbf{Y}^T[\mathbf{n}]\mathbf{Y}[\mathbf{n}])^{-1}\mathbf{Y}^T[\mathbf{n}]\mathbf{K}. \tag{15}$$

However, considering the fact that the introduction of an overdetermined set of stripes pursues the minimization of phase interferences, which introduce outliers when performing the HARP image gradient computation, our proposal is to resort to the Least Absolute Deviation (LAD) method, due to its robustness (Cordero-Grande and Alberola-López, 2012). Hence, the reconstruction is performed iteratively by:

$$\mathbf{F}_{l+1}[\mathbf{n}] = (\mathbf{Y}^T[\mathbf{n}]\mathbf{W}_l[\mathbf{n}]\mathbf{Y}[\mathbf{n}])^{-1}\mathbf{Y}^T[\mathbf{n}]\mathbf{W}_l[\mathbf{n}]\mathbf{K}, \tag{16}$$

with $\mathbf{W}_l[\mathbf{n}]$ a diagonal weight matrix obtained, at iteration l, by:

$$W_l^{jj}[\mathbf{n}] = \frac{1}{\sqrt{\sum_{h=1}^{2}\left(K^{jh} - \sum_{g=1}^{2}Y^{jg}[\mathbf{n}]F_l^{gh}[\mathbf{n}]\right)^2}} \tag{17}$$

and establishing $\mathbf{F}_0[\mathbf{n}] = \mathbf{I}$, with $\mathbf{I}$ the identity matrix. An analogous set of equations could be used to estimate $\mathbf{f}[\mathbf{n}]$.

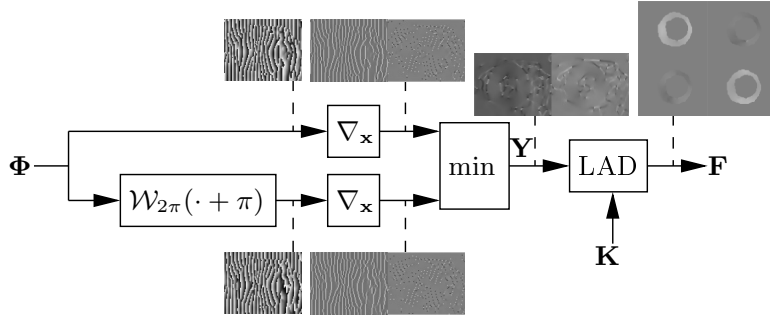The whole procedure is sketched in Figure 2.

Figure 2: Flowchart of the material deformation gradient tensor estimation. The LAD step is only performed inside the myocardial region (see Section 3 for a description of how this region is defined in our experiments) to avoid numerical instabilities due to unreliable tagging information outside the myocardium (due to fading and fluid motion). For those steps in which a vectorial or tensorial signal is generated, the different components are represented as different images. An exemplary modulation orientation is represented for those steps in which all the modulation components should be considered.

2.3. Green-Lagrange strain tensor

The target for standard myocardial motion analysis is to estimate the Green-Lagrange strain tensor $\mathbf{E}$, which is defined by:

$$\mathbf{E}[\mathbf{n}] = \frac{1}{2}(\mathbf{F}^T[\mathbf{n}]\mathbf{F}[\mathbf{n}] - \mathbf{I}), \tag{18}$$

Once $\mathbf{E}[\mathbf{n}]$ is estimated, we can compute its radial, circumferential and shearing components by contraction:

$$
\begin{aligned}
E_{\mathbf{RR}}[\mathbf{n}] &= \mathbf{R}^T[\mathbf{n}]\mathbf{E}[\mathbf{n}]\mathbf{R}[\mathbf{n}] \\
E_{\mathbf{CC}}[\mathbf{n}] &= \mathbf{C}^T[\mathbf{n}]\mathbf{E}[\mathbf{n}]\mathbf{C}[\mathbf{n}] \\
E_{\mathbf{RC}}[\mathbf{n}] &= \mathbf{R}^T[\mathbf{n}]\mathbf{E}[\mathbf{n}]\mathbf{C}[\mathbf{n}],
\end{aligned}
\tag{19}
$$

using the material polar coordinate system $(\mathbf{R}, \mathbf{C})$. Usually, one is interested in the so-called Green-Lagrange ejection strain which is the one that relates the maximum deformation at End-Systole (ES) with the reference configuration at End-Diastole (ED). Thus, for calculating the aforementioned descriptor, the above procedure should be applied to the ES cardiac phase. Otherwise, it should be repeated for each phase in order to obtain a full description of the mechanical behaviour of the myocardium along the cardiac cycle.

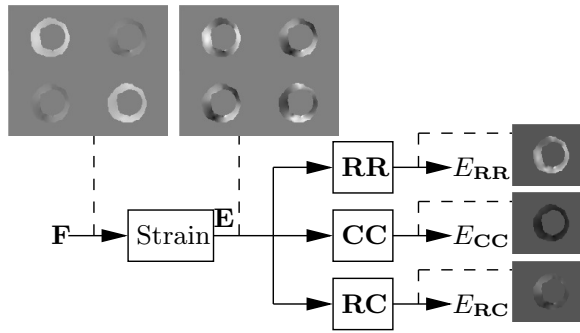The Green-Lagrange strain components computation is sketched in Figure 3.

Figure 3: Flowchart of the Green-Lagrange strain components calculation. For those steps in which a tensorial signal is generated, the different components are represented as different images.

3. Materials and methods

For the validation of the proposed approach on real data, we have acquired a medial slice on an adult volunteer using a MR SPAMM SENSitivity Encoding (SENSE) Turbo Field Echo (TFE) sequence on a Philips Achieva 3T scanner. The image has a spatial resolution of $1.333 \times 1.333 \, \text{mm}^2$ and a slice thickness of $8 \, \text{mm}$. The acquisition parameters are $T_E = 3.634 \, \text{ms}$, $T_R = 6.018 \, \text{ms}$ and flip angle $\alpha = 10°$. Regarding the tagging parameters, we validate the method for a fixed tag spacing of $k_i = k = 1/\lambda$, with $\lambda = 7 \, \text{mm}$ and compare the results of acquiring different number of orientations $u_i = (\cos(\theta_i), \sin(\theta_i))$ for the stripes. Similar experiments to the ones presented here could be carried out to compare the results of varying the tag spacing of the acquired SPAMM sequences —see Cordero-Grande and Alberola-López (2012) for some synthetic experiments in this regard— but in this paper we have preferred to focus on studying the effect of introducing an overdetermined set of orientations, as the reconstruction design becomes simpler in this case. We have also acquired a SENSE balanced TFE cine sequence with a spatial resolution of $1.25 \times 1.25 \, \text{mm}^2$, a slice thickness of $8 \, \text{mm}$, $T_E = 1.663 \, \text{ms}$, $T_R = 3.325 \, \text{ms}$ and $\alpha = 45°$. The cine sequence is acquired at the same slice location as the tagging sequence. The myocardium is segmented at ED and ES for the cine sequence and at ED for all the acquired orientations of the tagging sequence. The cine segmentation at ED is used to align the tagging orientations to a common reference system to correct for patient motion. The ES segmentation is used to define a region of interest on which to compute meaningful measures of the strain.

In the first experiment (Section 4.1) we use the number and orientations of the stripes that are shown in Table 1, which are selected to fully span the plane uniformly for each set. This seems a natural choice both to promote maximally incoherent interferences between the anatomical information and the deformed modulation pattern and to optimally condition the inversion problem in (16).

The validation is carried out using the estimates of the material deformation gradient tensor $\mathbf{F}^I$ at ES for each stripe set and value of I indicated before. Ideally, the tensors should be equal for all the studied cases. Therefore, a natural measure of the *reproducibility* of the estimation method for a predefined value of I would be the similarity between the estimated tensors from both sets with number of stripes I. To that end, we have used the Frobenius Norm Difference (FND) of the tensors obtained from the two

	$I=2$		$I=3$		
Set 1	$\theta_1 = 0°$	$\theta_2 = 90°$	$\theta_1 = -30°$	$\theta_2 = 30°$	$\theta_3 = 90°$
Set 2	$\theta_1 = -45°$	$\theta_2 = 45°$	$\theta_1 = -60°$	$\theta_2 = 0°$	$\theta_3 = 60°$

	$I=6$		$I=9$		
Set 1	$\theta_1 = -60°$	$\theta_4 = 30°$	$\theta_1 = -70°$	$\theta_4 = -10°$	$\theta_7 = 50°$
	$\theta_2 = -30°$	$\theta_5 = 60°$	$\theta_2 = -50°$	$\theta_5 = 10°$	$\theta_8 = 70°$
	$\theta_3 = 0°$	$\theta_6 = 90°$	$\theta_3 = -30°$	$\theta_6 = 30°$	$\theta_9 = 90°$
Set 2	$\theta_1 = -75°$	$\theta_4 = 15°$	$\theta_1 = -80°$	$\theta_4 = -20°$	$\theta_7 = 40°$
	$\theta_2 = -45°$	$\theta_5 = 45°$	$\theta_2 = -60°$	$\theta_5 = 0°$	$\theta_8 = 60°$
	$\theta_3 = -15°$	$\theta_6 = 75°$	$\theta_3 = -40°$	$\theta_6 = 20°$	$\theta_9 = 80°$

	$I=18$					
Set 1	$\theta_1 = -80°$	$\theta_4 = -50°$	$\theta_7 = -20°$	$\theta_{10} = 10°$	$\theta_{13} = 40°$	$\theta_{16} = 70°$
	$\theta_2 = -70°$	$\theta_5 = -40°$	$\theta_8 = -10°$	$\theta_{11} = 20°$	$\theta_{14} = 50°$	$\theta_{17} = 80°$
	$\theta_3 = -60°$	$\theta_6 = -30°$	$\theta_9 = 0°$	$\theta_{12} = 30°$	$\theta_{15} = 60°$	$\theta_{18} = 90°$
Set 2	$\theta_1 = -85°$	$\theta_4 = -55°$	$\theta_7 = -25°$	$\theta_{10} = 5°$	$\theta_{13} = 35°$	$\theta_{16} = 65°$
	$\theta_2 = -75°$	$\theta_5 = -45°$	$\theta_8 = -15°$	$\theta_{11} = 15°$	$\theta_{14} = 45°$	$\theta_{17} = 75°$
	$\theta_3 = -65°$	$\theta_6 = -35°$	$\theta_9 = -5°$	$\theta_{12} = 25°$	$\theta_{15} = 55°$	$\theta_{18} = 85°$

Table 1: Stripe orientations used in experiment 1.

stripe sets at a given I:

$$\mathrm{FND}^I(\mathbf{x}) = \sqrt{\sum_{m=1}^{2}\sum_{n=1}^{2}(F_{mn}^{I,1}(\mathbf{x}) - F_{mn}^{I,2}(\mathbf{x}))^2}. \qquad (20)$$

Hence, for each I we generate a FND distribution using the pixels inside the myocardium. Consequently, we have carried out MannWhitney U-tests to find significant differences in the median —subsequently denoted by $\nu(\mathrm{FND})$— of these distributions. Additionally, we measure the percentage of improvement in the median reproducibility when introducing a larger number of stripes.

As for the second experiment (Section 4.2), we have tested whether a larger reproducibility can be achieved by repeated acquisition of certain stripe orientations or, alternatively, by extending the stripe set to span the orientation space uniformly. To that end, we have obtained the same FND distribution as in the preceding experiment but now considering the stripe sets included in Table 2. Once again, we pursue to find significant differences in the medians of the distributions involved and measure the median reproducibility improvement.

A synthetic experiment (Section 4.3) is performed to aid the interpretation of results on real data. An incompressible radially varying deformation has been applied over the magnetization patterns according to $r =$

	I = 6 with repeated orientations			I = 6 spanning the plane		
Set 1	$\theta_1 = 0°$	$\theta_3 = 0°$	$\theta_5 = 90°$	$\theta_1 = -60°$	$\theta_3 = 0°$	$\theta_5 = 60°$
	$\theta_2 = 0°$	$\theta_4 = 90°$	$\theta_6 = 90°$	$\theta_2 = -30°$	$\theta_4 = 30°$	$\theta_6 = 90°$
Set 2	$\theta_1 = -45°$	$\theta_3 = -45°$	$\theta_5 = 45°$	$\theta_1 = -75°$	$\theta_3 = -15°$	$\theta_5 = 45°$
	$\theta_2 = -45°$	$\theta_4 = 45°$	$\theta_6 = 45°$	$\theta_2 = -45°$	$\theta_4 = 15°$	$\theta_6 = 75°$

Table 2: Stripe orientations used in experiment 2.

$\sqrt{R^2 - \gamma R_{\mathrm{i}}^2}$, where r is the radial spatial coordinate (after applying the deformation), R is the radial material coordinate, γ is a parameter that accounts for the degree of deformation applied, and R_{i} is the inner radius of an annulus taken as a reference of the myocardial structure. In our experiment we have generated an image of size 192×192, with an annulus given by $R_{\mathrm{i}} = 28$ and $R_{\mathrm{o}} = 40$, with R_{o} its outer radius. The spacing of the tags is given by $\lambda = 7.15$. Four strain estimation procedures are compared using the combinations of the minimum number of orientations ($I = 2$) versus a large number of orientations ($I = 36$) and non-windowed versus windowed local phase estimation. We refer to these methods as HARP ($I = 2$ / non-windowed), WHARP ($I = 2$ / windowed), MOHARP ($I = 36$ / non-windowed), and MOWHARP ($I = 36$ / windowed)[2]. As in all other experiments, the HARP analysis for $I > 2$ is performed by using the conventional HARP filter to estimate the local phase and the proposed LAD deformation gradient tensor estimator.

Finally, for visual illustration we show the results of the application of the method to the stripe sets included in Table 3 (Section 4.4).

Regarding implementation details, in accordance with the discussion and experiments in Cordero-Grande et al. (2011), we have resorted to an analysis Gaussian window w of size $\mathbf{Q} = [32, 32]$. Its expression, up to a proportionality factor to ensure its unit norm, is

$$w[\mathbf{n}] \propto e^{-8 \sum\limits_{j=1}^{2} \left(\frac{n^j}{Q^j - 1} \right)^2},$$ (21)

where the factor 8 guarantees that the truncation occurs where the window values are close to zero. On the other side, we have used a circumferential spectral filter H with radius r centered, at a given spatial location, at the

---

[2]To refer to methods using $I > 2$ orientations we will use the prefix MO or specify the number of orientations depending on the level of information required.

I = 2			I = 3			
$\theta_1 = 0°$	$\theta_2 = 90°$		$\theta_1 = -60°$	$\theta_2 = 0°$	$\theta_3 = 60°$	
I = 4			**I = 6**			
$\theta_1 = -45°$	$\theta_3 = 45°$		$\theta_1 = -60°$	$\theta_3 = 0°$	$\theta_5 = 60°$	
$\theta_2 = 0°$	$\theta_4 = 90°$		$\theta_2 = -30°$	$\theta_4 = 30°$	$\theta_6 = 90°$	
I = 9			**I = 12**			
$\theta_1 = -80°$	$\theta_4 = -20°$	$\theta_7 = 40°$	$\theta_1 = -75°$	$\theta_4 = -30°$	$\theta_7 = 15°$	$\theta_{10} = 60°$
$\theta_2 = -60°$	$\theta_5 = 0°$	$\theta_8 = 60°$	$\theta_2 = -60°$	$\theta_5 = -15°$	$\theta_8 = 30°$	$\theta_{11} = 75°$
$\theta_3 = -40°$	$\theta_6 = 20°$	$\theta_9 = 80°$	$\theta_3 = -45°$	$\theta_6 = 0°$	$\theta_9 = 45°$	$\theta_{12} = 90°$
I = 18						
$\theta_1 = -80°$	$\theta_4 = -50°$	$\theta_7 = -20°$	$\theta_{10} = 10°$	$\theta_{13} = 40°$	$\theta_{16} = 70°$	
$\theta_2 = -70°$	$\theta_5 = -40°$	$\theta_8 = -10°$	$\theta_{11} = 20°$	$\theta_{14} = 50°$	$\theta_{17} = 80°$	
$\theta_3 = -60°$	$\theta_6 = -30°$	$\theta_9 = 0°$	$\theta_{12} = 30°$	$\theta_{15} = 60°$	$\theta_{18} = 90°$	
I = 36						
$\theta_1 = -85°$	$\theta_7 = -55°$	$\theta_{13} = -25°$	$\theta_{19} = 5°$	$\theta_{25} = 35°$	$\theta_{31} = 65°$	
$\theta_2 = -80°$	$\theta_8 = -50°$	$\theta_{14} = -20°$	$\theta_{20} = 10°$	$\theta_{26} = 40°$	$\theta_{32} = 70°$	
$\theta_3 = -75°$	$\theta_9 = -45°$	$\theta_{15} = -15°$	$\theta_{21} = 15°$	$\theta_{27} = 45°$	$\theta_{33} = 75°$	
$\theta_4 = -70°$	$\theta_{10} = -40°$	$\theta_{16} = -10°$	$\theta_{22} = 20°$	$\theta_{28} = 50°$	$\theta_{34} = 80°$	
$\theta_5 = -65°$	$\theta_{11} = -35°$	$\theta_{17} = -5°$	$\theta_{23} = 25°$	$\theta_{29} = 55°$	$\theta_{35} = 85°$	
$\theta_6 = -60°$	$\theta_{12} = -30°$	$\theta_{18} = 0°$	$\theta_{24} = 30°$	$\theta_{30} = 60°$	$\theta_{36} = 90°$	

Table 3: Stripe orientations used for visual illustration.

maximum of the spectra $\hat{\mathbf{k}}[\mathbf{m}]$ (i.e., the *ridge* of the WFT) in the surroundings of the reference spatial frequency of the tags $\mathbf{k}_i$, which is computed by considering a region $\{\mathbf{k} : 0.6k_i < k < 1.4k_i \wedge |\angle\mathbf{k} - \theta_i| < \pi/6\}$. Hence, we can write the filter parameters as $\boldsymbol{\lambda}[\mathbf{m}] = (\hat{\mathbf{k}}[\mathbf{m}], r)$. Defining a radial variable with center $\hat{\mathbf{k}}[\mathbf{m}]$ and normalized to the bandwidth r, $\rho[\mathbf{q}] = |\mathbf{q} - \hat{\mathbf{k}}[\mathbf{m}]|/r$, the filter reads:

$$H^{\boldsymbol{\lambda}[\mathbf{m}]}[\mathbf{q}] = \begin{cases} 1 & \text{if } \rho[\mathbf{q}] \leq 1 \\ e^{-\frac{(\rho[\mathbf{q}]-1)^2}{2\sigma^2}} & \text{otherwise,} \end{cases} \tag{22}$$

with $\sigma = 0.05$ typically. We can normalize the filter bandwidth with respect to the wave number of the applied modulation by using the parameter $\mu = r/k$. In the experiments we have tested the values of the filter bandwidth given by $\mu_b = 0.05 + 0.05b$, with $1 \leq b \leq 11$, therefore with $0.1 \leq \mu_b \leq 0.6$.

4. Results

4.1. Reproducibility of increased number of orientations

In Figure 4a we show the results of $\nu(\text{FND})$ for the sets included in Table 1 both for the application of the HARP and the WHARP analysis for

the range of values of μ considered whereas in Figure 4b the corresponding FND Cumulative Distribution Function (CDF) for $\mu = 0.35$ is shown. The results included in Figure 4a confirm our hypothesis that increasing the

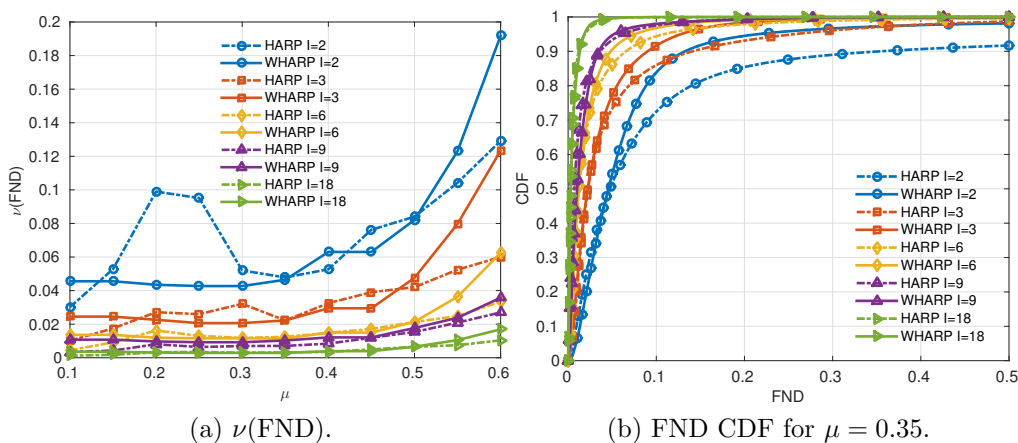(a) ν(FND).   (b) FND CDF for $\mu = 0.35$.

Figure 4: FND for the sets considered in Table 1 (different number of orientations) using both windowed and non-windowed analysis.

number of orientations increases the reproducibility of the strain measurements as assessed by the median of the FND calculated from two settings of the orientations set. The decrease in the median of the FND when increasing the number of orientations is consistent against changes in the filter bandwidth μ and the use of either the FT (HARP method) or the WFT (WHARP method). The results in Figure 4b suggest that there is also a consistent improvement in the reproducibility when assessed by the whole range of quantiles of the FND distribution. Regarding the differences between the MOHARP and MOWHARP methods, no conclusions can be established about their respective reproducibilities from this experiment.

In Figure 5 we show the probability density function (PDF) of the $E_{\mathbf{RR}}$, $E_{\mathbf{CC}}$ and $E_{\mathbf{RC}}$ strain components for the sets considered in Table 1 for $\mu = 0.35$ both for the application of the HARP and the WHARP analysis. From Figure 5a, the differences in the estimated $E_{\mathbf{RR}}$ between both methods appear to be appreciable. The HARP method seems to largely underestimate the radial component of the strain tensor, a shortcoming that has been previously reported (Parthasarathy, 2006), whereas the values of the WHARP method seem closer to the ones expected in an adult volunteer. Although this effect is partly due to the bandwidth used in this experiment,

15

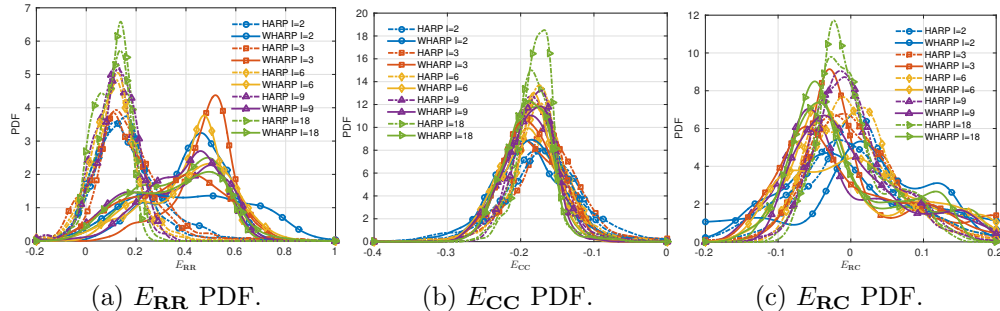(a) $E_{\mathbf{RR}}$ PDF.   (b) $E_{\mathbf{CC}}$ PDF.   (c) $E_{\mathbf{RC}}$ PDF.

Figure 5: Strain PDF for the sets considered in Table 1 (different number of orientations) for $\mu = 0.35$ using both windowed and non-windowed analysis.

the crucial point is that even if the reproducibility of both methods seems to be similar, the actual measures obtained by both might greatly differ. We will perform a simulation based study of this effect in Section 4.3. This inconsistency in the estimated measurements seems to largely disappear for the $E_{\mathbf{CC}}$ component (Figure 5b) and substantially diminish for the $E_{\mathbf{RC}}$ (Figure 5c). Additionally, no important systematic errors in the estimated distributions are visually observed for this bandwidth when changing the number of orientations.

Finally, in Table 4 we include the results of the Mann Whitney U-tests on the FND distributions of different number of orientations when applying the MOWHARP technique for some of the considered μ values. Moreover, the percentage of median reproducibility improvement in strain estimates when acquiring new orientations is also provided for every pair of compared number of stripes. These results further support that increasing the number of orientations increases the reproducibility of the strain measurements as suggested in Figure 4a. Additionally, also from Table 4, we observe the percentage of improvement in the median reproducibility to be noteworthy, which is due to the strong artifacts produced by the HARP and WHARP methods.

4.2. Reproducibility of repeated measurements versus extended orientations

In Figure 6a we show the results of $\nu(\text{FND})$ for the sets included in Table 2 both for the application of the MOHARP and the MOWHARP methods for the range of values of μ considered, whereas in Figure 6b the corresponding FND CDF for $\mu = 0.35$ is shown. Analogously to the results

		$I_1 = 2$	$I_1 = 3$	$I_1 = 6$	$I_1 = 9$
$\mu = 0.15$	$I_2 = 3$	2.1 / $< 10^{-9}$ / 46	—	—	—
	$I_2 = 6$	3.2 / $< 10^{-9}$ / 70	1.1 / $< 10^{-9}$ / 45	—	—
	$I_2 = 9$	3.4 / $< 10^{-9}$ / 76	1.3 / $< 10^{-9}$ / 55	0.2 / $1 \cdot 10^{-7}$ / 18	—
	$I_2 = 18$	4.2 / $< 10^{-9}$ / 92	2.1 / $< 10^{-9}$ / 85	1.0 / $< 10^{-9}$ / 73	0.7 / $< 10^{-9}$ / 67
$\mu = 0.25$	$I_2 = 3$	2.1 / $< 10^{-9}$ / 50	—	—	—
	$I_2 = 6$	3.1 / $< 10^{-9}$ / 73	0.9 / $< 10^{-9}$ / 45	—	—
	$I_2 = 9$	3.3 / $< 10^{-9}$ / 80	1.2 / $< 10^{-9}$ / 59	0.3 / $1 \cdot 10^{-8}$ / 25	—
	$I_2 = 18$	3.9 / $< 10^{-9}$ / 93	1.8 / $< 10^{-9}$ / 86	0.9 / $< 10^{-9}$ / 75	0.6 / $< 10^{-9}$ / 67
$\mu = 0.35$	$I_2 = 3$	2.4 / $< 10^{-9}$ / 52	—	—	—
	$I_2 = 6$	3.5 / $< 10^{-9}$ / 75	1.0 / $< 10^{-9}$ / 48	—	—
	$I_2 = 9$	3.6 / $< 10^{-9}$ / 79	1.2 / $< 10^{-9}$ / 56	0.2 / $2 \cdot 10^{-6}$ / 16	—
	$I_2 = 18$	4.3 / $< 10^{-9}$ / 94	1.9 / $< 10^{-9}$ / 87	0.9 / $< 10^{-9}$ / 75	0.7 / $< 10^{-9}$ / 71
$\mu = 0.45$	$I_2 = 3$	3.3 / $< 10^{-9}$ / 53	—	—	—
	$I_2 = 6$	4.8 / $< 10^{-9}$ / 76	1.4 / $< 10^{-9}$ / 48	—	—
	$I_2 = 9$	5.1 / $< 10^{-9}$ / 81	1.7 / $< 10^{-9}$ / 59	0.3 / $7 \cdot 10^{-5}$ / 21	—
	$I_2 = 18$	5.9 / $< 10^{-9}$ / 94	2.6 / $< 10^{-9}$ / 87	1.1 / $< 10^{-9}$ / 74	0.8 / $< 10^{-9}$ / 68
$\mu = 0.55$	$I_2 = 3$	4.2 / $< 10^{-9}$ / 34	—	—	—
	$I_2 = 6$	8.6 / $< 10^{-9}$ / 70	4.4 / $< 10^{-9}$ / 54	—	—
	$I_2 = 9$	10.0 / $< 10^{-9}$ / 81	5.8 / $< 10^{-9}$ / 71	1.4 / $< 10^{-9}$ / 37	—
	$I_2 = 18$	11.2 / $< 10^{-9}$ / 91	7.1 / $< 10^{-9}$ / 87	2.6 / $< 10^{-9}$ / 71	1.3 / $< 10^{-9}$ / 54

Table 4: Mann Whitney U-tests on the FND distributions among different number of orientations I_1 (columns) and I_2 (rows). Left: $\nu(\mathrm{FND})^{I_1} - \nu(\mathrm{FND})^{I_2} (\%)$. Center: P-value. Right: $(\nu(\mathrm{FND})^{I_1} - \nu(\mathrm{FND})^{I_2})/\nu(\mathrm{FND})^{I_1} (\%)$.

presented in Section 4.1, from Figure 6a we can see that the reproducibility is increased when extending the orientation set with regard to repeating the measurements for the same total number of acquired orientations and therefore same acquisition time. In this case one also encounters that the results are consistent against changes in μ and the use of either the MOHARP or MOWHARP methods and when assessed not just in terms of the median but of the whole range of quantiles of the FND distribution, as reflected in Figure 6b.

In Figure 7 we show the PDF of the $E_{\mathbf{RR}}$, $E_{\mathbf{CC}}$ and $E_{\mathbf{RC}}$ strain components for the sets considered in Table 2 for $\mu = 0.35$ both for the application of the MOHARP and the MOWHARP methods. Comments included in Section 4.1 about the reproducibility and discrepancies between the MOHARP and MOWHARP methods also apply to this case.

Finally, in Table 5 we include the results of the Mann Whitney U-tests on the FND distributions of repeated measurements versus extended orientations for the application of the MOWHARP analysis for some of the considered μ values. Moreover, a measure of the median reproducibility improvement obtained when acquiring an extended set of orientations is also

(a) $\nu(\text{FND})$.
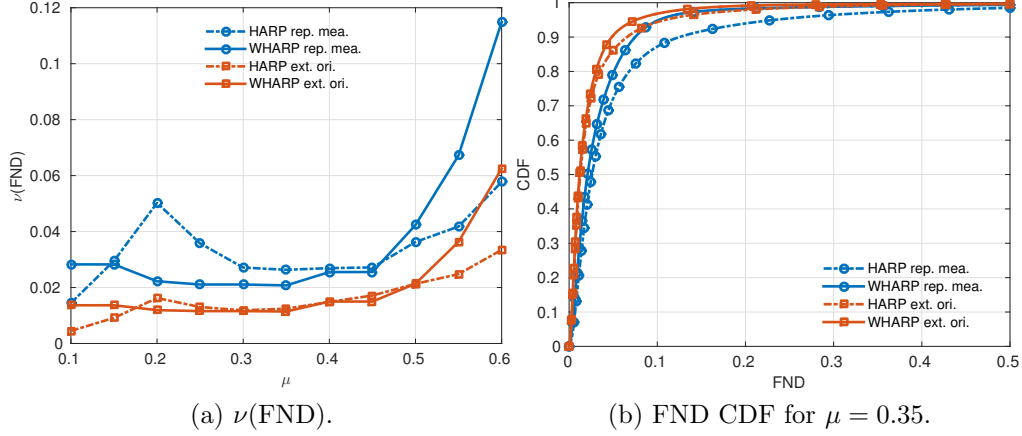
(b) FND CDF for $\mu = 0.35$.
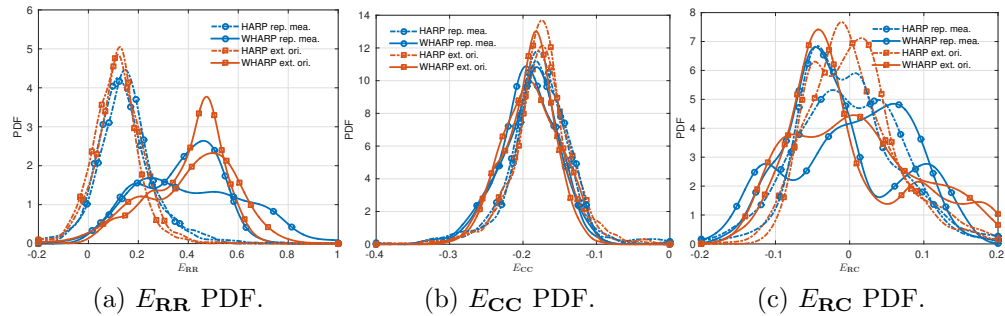
Figure 6: FND for the sets considered in Table 2 (repeated measurements / extended orientations) using both non-windowed and windowed analysis.

provided. Interestingly, we observe that, for the number of orientations stud-

$\mu = 0.15$	$\mu = 0.25$	$\mu = 0.35$	$\mu = 0.45$	$\mu = 0.55$
1.4 / $< 10^{-9}$ / 51	1.0 / $< 10^{-9}$ / 46	0.9 / $< 10^{-9}$ / 44	1.0 / $< 10^{-9}$ / 41	3.2 / $< 10^{-9}$ / 46

Table 5: Mann Whitney U-tests on the FND distributions between different orientation configurations. Left: $\nu(\text{FND}^{\text{ra}}) - \nu(\text{FND}^{\text{eo}})(\%)$ with FND^{ra} denoting the case with repeated angles and FND^{eo} the one with extended orientations. Center: P-value. Right: $(\nu(\text{FND})^{\text{ra}} - \nu(\text{FND})^{\text{eo}})/\nu(\text{FND})^{\text{ra}}(\%)$.

ied in this experiment, the strategy here proposed is able to almost double the

(a) $E_{\mathbf{RR}}$ PDF.

(b) $E_{\mathbf{CC}}$ PDF.

(c) $E_{\mathbf{RC}}$ PDF.

Figure 7: Strain PDF for the sets considered in Table 2 (repeated measurements / extended orientations) for $\mu = 0.35$ using both non-windowed and windowed analysis.

18

reproducibility of the obtained estimations. Moreover, the results are consistent against changes of μ. Improved reproducibility when using an extended set of orientations than when repeating the measurements for the same orientations is a key feature of the MOWHARP method, as it demonstrates the prominence of orientation dependent artifacts with respect to noise for standard HARP reconstructions. Further insight into this property is given in the synthetic experiment that follows.

4.3. Validation on synthetic data

Sections 4.1 and 4.2 have shown the ability of the proposed acquisition of an extended set of stripe orientations to improve the reproducibility of strain estimations using both the MOHARP and MOWHARP techniques. However, the results in Figures 5 and 7 show that there is a significant difference in the strain estimations given by both techniques, especially in the radial case. Thus, a synthetic experiment has been conducted to justify our claims about the bias reduction when using the windowed analysis as well as to illustrate about the demonstrated advantages of multi-orientation for real data.

An incompressible radially varying deformation has been applied over the magnetization patterns as described in Section 3. We have assumed no structure is present in the underlying image so as to avoid the artifacts provoked by interferences from the anatomical component, which simplifies the interpretation of results. Thus, the annular region is used to study the difference between the estimated ($\hat{\mathbf{E}}$) and the ground truth ($\mathbf{E}$) strain, not as an anatomical model. The bandwidth of the BP filters applied is set to $\mu = 0.35$.

First, the estimation variance, $\text{var}(\hat{E})$, for each of the strain components is calculated as the difference between the mean squared error, $\text{MSE}(\hat{E})$, and the squared estimation bias, $(B(\hat{E}))^2$, and plotted in a logarithmic scale. Results are shown in Figure 8. For small deformations, the estimation variance remains negligible for all methods. As the deformation gets larger, a transition point is reached in which the $I = 2$ methods (HARP/WHARP) are no longer able to provide meaningful estimates of the strain so that the estimation variance explodes. From the curves in Figure 8, the transition point for this experiment could be located around deformation levels of $\gamma = 0.35$ for HARP and $\gamma = 0.5$ for WHARP and it remains approximately the same for the different strain components. The huge variance of

the recovered strain for large deformations is provoked by the artifacts introduced by certain components of the strain modulation being discarded by BP filtering. However, in our view, when using a large number of orientations (MOHARP/MOWHARP), these artifacts appear incoherently distributed circumferentially, so that, by using the LAD estimator, only those orientations that provide meaningful pointwise estimates of the deformation gradient tensor are effectively accounted for and the estimation remains stable. These results are consistent with the improved reproducibility of multi-oriented methods in real data, as shown in Sections 4.1 and 4.2.

(a) $\mathrm{Var}(\hat{E}_{\mathbf{RR}})$.   (b) $\mathrm{Var}(\hat{E}_{\mathbf{CC}})$.   (c) $\mathrm{Var}(\hat{E}_{\mathbf{RC}})$.
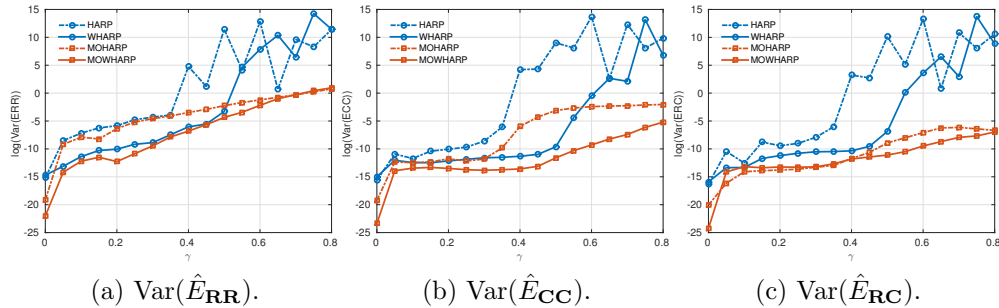
Figure 8: Strain estimation variance (in a logarithmic scale) for different degrees of deformation and $\mu = 0.35$.

Second, the estimation bias, $B(\hat{E})$, is calculated for stable estimators (MOHARP/MOWHARP) and shown in Figure 9. In this case, we see that both are unbiased for small deformations but, once again, after a given transition point, both start to deviate from the ground truth. This also can be attributed to discarded spectral components of the strain. Namely, $\hat{E}_{\mathbf{RR}}$ (positive) and $\hat{E}_{\mathbf{CC}}$ (negative) are biased towards zero, whereas no bias is observed in $\hat{E}_{\mathbf{RC}}$ because it is identically zero in our phantom. However, due to its ability to follow the spatial variation of the orientation and spacing of the tag pattern, the bias of the MOWHARP method remains consistently lower. These results are in accordance with the shift towards zero observed for HARP and MOHARP estimations in Figures 5 and 7.

In this experiment, estimation errors are provoked by the bandwidth of the BP filter being too small to capture the frequency modulation introduced by the deformation. Thus, in this setting, they could be mitigated by increasing the bandwidth. However, in a more realistic scenario, artifacts coming from the anatomical signal will also influence the estimation and they will

(a) $B(\hat{E}_{\mathbf{RR}})$.   (b) $B(\hat{E}_{\mathbf{CC}})$.   (c) $B(\hat{E}_{\mathbf{RC}})$.
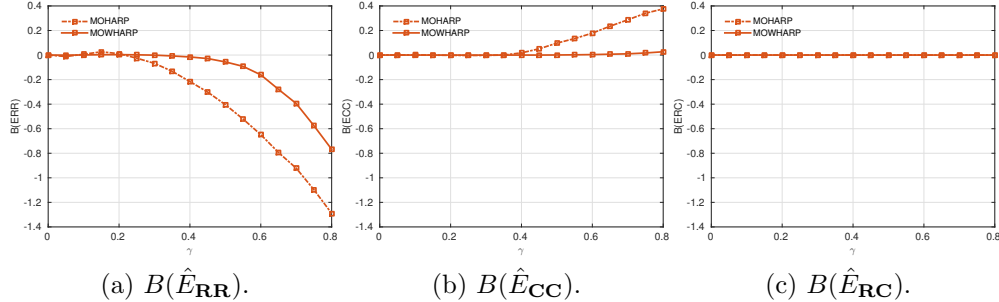
Figure 9: Strain estimation bias for different degrees of deformation and $\mu = 0.35$.

increase with increased bandwidths so that a satisfactory tradeoff is usually less likely for HARP than for MOWHARP. This is further investigated below by visual inspection of the estimations in real data.

4.4. Visual results

In Figures 10, 11 and 12 we respectively show the results of the $E_{\mathbf{RR}}$, $E_{\mathbf{CC}}$ and $E_{\mathbf{RC}}$ for some of the considered μ values and the set of orientations included in Table 3 both for the MOHARP and MOWHARP methods.

Visual results illustrate about the influence of the main parameters of our method in the reconstruction of the strain tensor from tagged MR images. From Figure 10a we can see that the result for the radial component of the strain by means of the HARP method ($I = 2$, left column) is unsatisfactory: when using small bandwidths μ the radial strain is underestimated whereas when incrementing μ significant artifacts start to appear. The emergence of artifacts is greatly limited by the use of a larger number of orientations but obviously at the price of increasing the acquisition time. When using MOWHARP (see Figure 10b) both undesirable effects seem to be appreciably diminished as the results appear more consistent among different bandwidths —additional related considerations were established in Cordero-Grande et al. (2011, 2014)—. Differences between both methods are observed even at large number of orientations, showing the fundamental limitation of the non-windowed analysis to recover large strains. Similar results are observed for the circumferential component of the strain in Figure 11 although acceptable results are obtained from MOHARP for both large I and μ in this case. Finally, the estimation of the radial-circumferential component of the strain in Figure 12 seems to stay somewhere in between the radial and

21
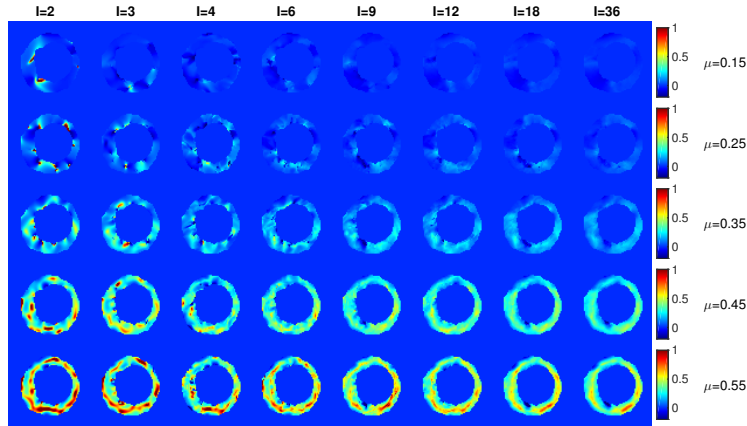
(a) $E_{\mathbf{RR}}$ strain: MOHARP.
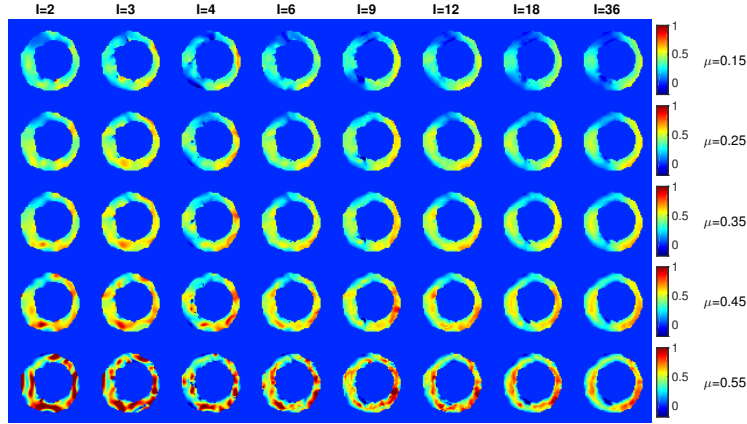
(b) $E_{\mathbf{RR}}$ strain: MOWHARP.

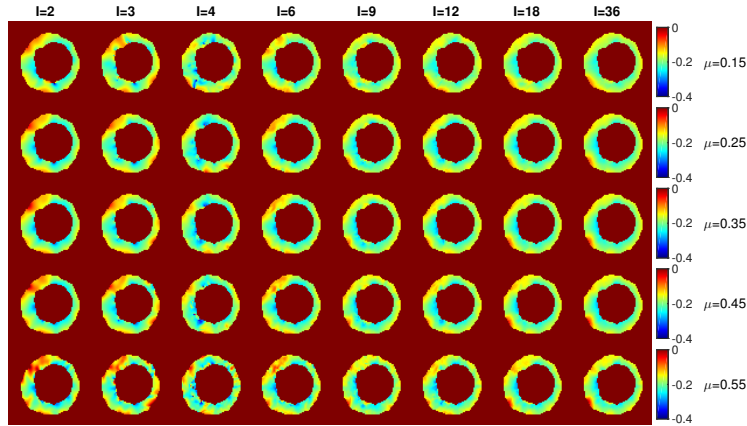Figure 10: $E_{\mathbf{RR}}$ strain for the sets included in Table 3.

circumferential estimates: biases introduced by the HARP analysis seem to be present but they are not so strong as in the radial case.

5. Discussion

From the results in Section 4 we can see that our methodology is effective in improving the robustness and accuracy when obtaining direct strain measurements from tagged MR sequences. Accuracy improvement is mostly based on the reconstruction technique adopted, where the FT is substituted by the WFT in order to better detect the local phase of the modulation
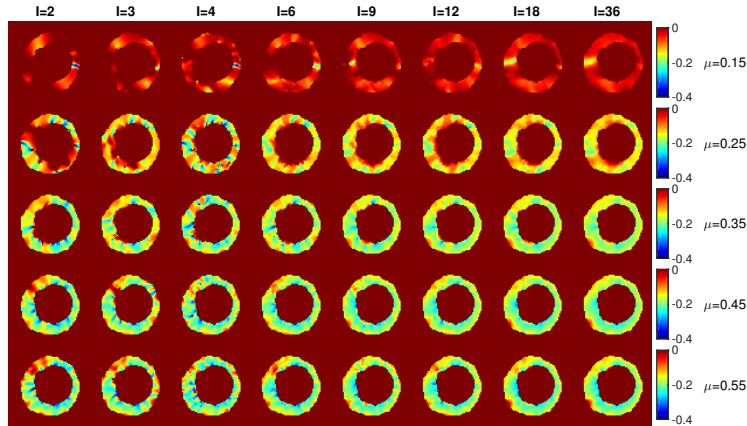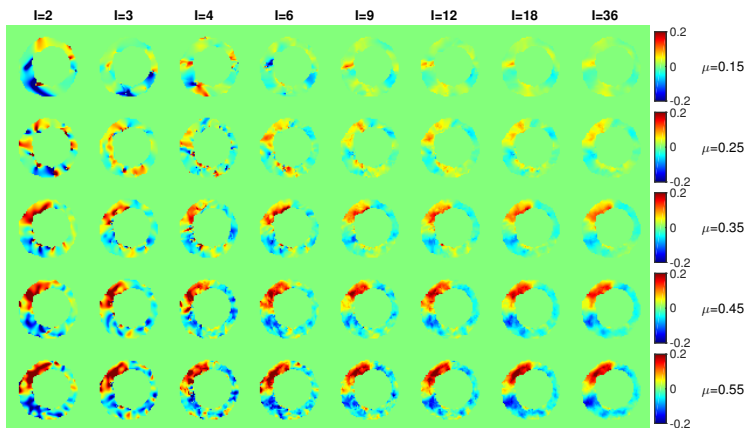
(a) $E_{\mathbf{CC}}$ strain: MOHARP.

(b) $E_{\mathbf{CC}}$ strain: MOWHARP.

Figure 11: $E_{\mathbf{CC}}$ strain for the sets included in Table 3.

pattern. On the other side, in the implementation here presented, the robustness improvement comes at the expense of introducing an overload in the acquisition time due to the need of acquiring different orientations of the modulated magnetization pattern.

Longer acquisition times (that, for naive acquisition extensions, vary linearly with the number of acquired orientations) would in turn increase the likelihood of other artifacts to affect the image quality, such as those arising in the presence of arrythmias or longer apneas. However, different techniques may be implemented to accelerate the acquisition of the modulations set. Probably the most important consideration to be kept in mind in this

23

(a) $E_{\mathbf{RC}}$ strain: MOHARP.
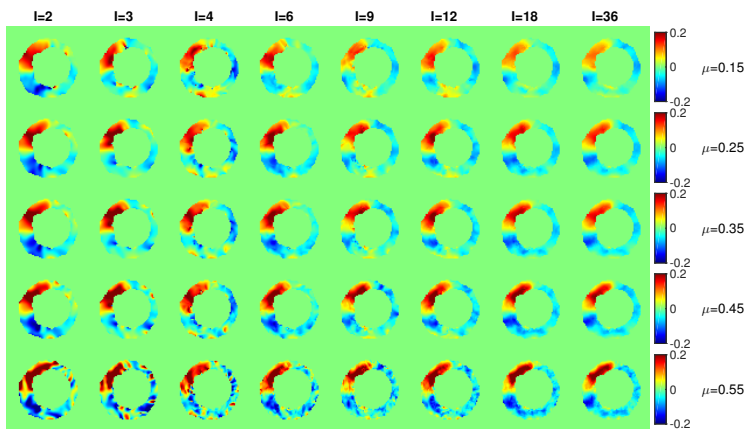
(b) $E_{\mathbf{RC}}$ strain: MOWHARP.

Figure 12: Strain components for the sets considered in Table 3.

regard is that only a reduced subset of the k-space, given by a region around the spectral peak, is needed to reconstruct the local phase using the HARP method (Sampath et al., 2003), which also holds in our extension. Additionally, different harmonics may be simultaneously acquired provided that their spectral peaks can be separated by a proper k-space filtering, which can subsequently accelerate the acquisition process (indeed, this idea is applied in grid-like and high order SPAMM acquisitions).

Important open tasks, specially for simultaneous multi-harmonic acquisition, would be the combined design of optimal analysis windows and BP filters, the automatic estimation of the BP filter bandwidth, and the de-

sign of optimal modulation sampling patterns if different tag spacings are to be sampled. Indeed, our reconstruction method could be readily applied to grid-like acquisitions, and, by designing adequate BP filters and using a straightforward extension of the proposed ridge detector, it may as well be extended to high order SPAMM analysis. However, additional local phase information will likely be counteracted by increased interferences, which may be difficult to balance. In this regard, extensions of the current methodology to diminish the influence of the anatomical signal on the demodulated deformations may also help in obtaining cleaner estimations.

Regarding reconstruction times, we believe the method is fully feasible for offline reconstructions to be used in clinical applications provided adequate hardware is available. On the one side, the most demanding computations (windowed local phase computation and LAD estimation) admit massive GPU accelerations. On the other side, considering computations are mostly performed on a pixelwise basis, the dimensions of the problem can be significantly reduced with a proper masking of the myocardial tissue. Namely, in our current implementation under MATLAB, windowed local phase computation (GPU-based) takes around $0.1\,\mathrm{s}$ per orientation and the LAD estimation (CPU-based) between $0.1\,\mathrm{s}$ ($I = 2$) and $1\,\mathrm{s}$ ($I = 36$).

All in all, we think that the proposed methodology brings new opportunities in the design of SPAMM acquisition sequences for HARP imaging, particularly when combined with modern acquisition protocols such as Ibrahim et al. (2006); Stoeck et al. (2012) and also considering that when the interest resides in measuring the mechanical properties of the myocardium, selective excitation methods may be adopted to reduce the field of view to be encoded. Although the 3D extension of the reconstruction pipeline in Section 2 would be conceptually straightforward, 3D SPAMM acquisition still presents significant challenges (Rutz et al., 2008; Stoeck et al., 2012). In addition, the design of optimal coverage of the orientation space might be more intricate than in the 2D case, particularly if attempted to be adapted to the myocardial geometry. On the other hand, we believe that the ideas here introduced might also be useful for Displacement ENcoding with Stimulated Echoes (Kuijer et al., 2006) (DENSE) or even Phase Contrast (PC) acquisitions.

Finally, we would like to stress that the acquisition extension we propose in this paper, i.e., that of gathering an overdetermined set of modulations in order to improve the robustness of strain estimation, is not so evident as it may appear at first glance. The reason is that this extension is not just based on gathering a large amount of data so as to avoid a noise-related

25

shortcoming of the measurement process, but it is devised to correct for the specific artifacts appearing in conventional HARP reconstruction. This can be noted by paying attention to the use of the LAD estimator instead of the LS one. A comparative study of the gain provided by both estimators in a synthetic dataset was developed in Cordero-Grande and Alberola-López (2012) and is not repeated here for the sake of conciseness, but the results conclusively supported the hypothesis that the LAD estimator is better suited for this reconstruction problem.

6. Conclusions

A method for the reconstruction of the strain tensor in tagged MR sequences is presented which builds upon (1) the use of the WFT for an unbiased estimation of the local phase of the modulation pattern and (2) the acquisition of an overdetermined set of stripes in order to limit the influence of outliers derived from the combination of phase interferences and the gradient operation. The method has significantly improved both the accuracy and the reproducibility of myocardial deformation measurements with respect to a standard acquisition in which just two orthogonal orientations are acquired and a standard HARP analysis is performed. Taking the considerations included in Section 5 into account, new families of acquisition protocols can potentially be designed for motion sensitive MR imaging, which could simultaneously improve the resolution, robustness and precision in the analysis of motion.

References

Abd-Elmoniem, K.Z., Parthasarathy, V., Prince, J.L., 2006. Improving HARP cardiac strain mapping using nonlinear diffusion, in: 14th Proceedings of the International Society on Magnetic Resonance in Medicine, Seattle, USA. p. 1219.

Agarwal, H.K., Prince, J.L., Abd-Elmoniem, K.Z., 2010. Total removal of unwanted harmonic peaks (TruHARP) MRI for single breath-hold high-resolution myocardial motion and strain quantification. Magn. Reson. Med. 64, 574–585.

Axel, L., Dougherty, L., 1989. MR imaging of motion with spatial modulation of magnetization. Radiol 171, 841–845.

Axel, L., Montillo, A., Kim, D., 2005. Tagged magnetic resonance imaging of the heart: a survey. Med Image Anal 9, 376–393.

Bruurmijn, L.C.M., Kause, H.B., Filatova, O.G., Duits, R., Fuster, A., Florack, L.M.J., van Assen, H.C., 2013. Myocardial deformation from local frequency estimation in tagging MRI, in: 7th International Conference on Functional Imaging and Modeling of the Heart, London, UK. pp. 284–291.

Cordero-Grande, L., Alberola-López, C., 2012. Extending HARP imaging by acquiring an overdetermined set of stripes, in: 20th Proceedings of the International Society on Magnetic Resonance in Medicine, Melbourne, Australia. p. 4158.

Cordero-Grande, L., Royuela-del-Val, J., Martín-Fernández, M., Alberola-López, C., 2014. MOWHARP: Multi-oriented windowed HARP reconstruction for robust strain imaging, in: 22nd Proceedings of the International Society on Magnetic Resonance in Medicine, Milan, Italy. p. 7540.

Cordero-Grande, L., Vegas-Sánchez-Ferrero, G., Casaseca-de-la-Higuera, P., Alberola-López, C., 2011. Improving harmonic phase imaging by the windowed Fourier transform, in: 8th IEEE International Symposium on Biomedical Imaging: From Nano to Macro, Chicago, USA. pp. 520–523.

Crum, W.R., Berry, E., Ridgway, J.P., Sivananthan, U.M., Tan, L.B., Smith, M.A., 1998. Frequency-domain simulation of MR tagging. J Magn Reson Imaging 8, 1040–1050.

Fu, Y.B., Chui, C.K., Teo, C.L., 2013. Accurate two-dimensional cardiac strain calculation using adaptive windowed Fourier transform and Gabor wavelet transform. Int J Comput Assist Radiol Surg 8, 135–144.

Ibrahim, E.S.H., 2011. Myocardial tagging by cardiovascular magnetic resonance: evolution of techniques–pulse sequences, analysis algorithms, and applications. J Cardiovasc Magn Reson 13, 36.

Ibrahim, E.S.H., Stuber, M., Schär, M., Osman, N.F., 2006. Improved myocardial tagging contrast in cine balanced SSFP images. J Magn Reson Imaging 24, 1159–1167.

Jeung, M.Y., Germain, P., Croisille, P., El ghannudi, S., Roy, C., Gangi, A., 2012. Myocardial tagging with MR imaging: Overview of normal and pathologic findings. RadioGraphics 32, 1381–1398.

Jones, D.K., Horsfield, M.A., Simmons, A., 1999. Optimal strategies for measuring diffusion in anisotropic systems by magnetic resonance imaging. Magn. Reson. Med. 42, 515–525.

Kuijer, J.P.A., Hofman, M.B.M., Zwanenburg, J.J.M., Marcus, J.T., van Rossum, A.C., Heethaar, R.M., 2006. DENSE and HARP: Two views on the same technique of phase-based strain imaging. J Magn Reson Imaging 24, 1432–1438.

Kuijer, J.P.A., Jansen, E., Marcus, J.T., van Rossum, A.C., Heethaar, R.M., 2001. Improved harmonic phase myocardial strain maps. Magn. Reson. Med. 46, 993–999.

Osman, N.F., McVeigh, E.R., Prince, J.L., 2000. Imaging heart motion using harmonic phase MRI. IEEE Trans Med Imaging 19, 186–202.

Papadakis, N.G., Xing, D., Huang, C.L.H., Hall, L.D., Carpenter, T.A., 1999. A comparative study of acquisition schemes for diffusion tensor imaging using MRI. J Magn Reson 137, 67–82.

Parthasarathy, V., 2006. Characterization of Harmonic Phase MRI: Theory, Simulations, and Applications. Ph.D. thesis. The Johns Hopkins University. http://speech.umaryland.edu/publications/vijay_dissertation.pdf.

Rutz, A.K., Ryf, S., Plein, S., Boesiger, P., Kozerke, S., 2008. Accelerated whole-heart 3D CSPAMM for myocardial motion quantification. Magn Reson Med 59, 755–763.

Sampath, S., Derbyshire, J.A., Atalar, E., Osman, N.F., Prince, J.L., 2003. Real-time imaging of two-dimensional cardiac strain using a harmonic phase magnetic resonance imaging (HARP-MRI) pulse sequence. Magn Reson Med 50, 154–163.

Shehata, M.L., Cheng, S., Osman, N.F., Bluemke, D.A., Lima, J.A., 2009. Myocardial tissue tagging with cardiovascular magnetic resonance. J Cardiovasc Magn Reson 11, 55.

Simpson, R.M., Keegan, J., Firmin, D.N., 2013. MR assessment of regional myocardial mechanics. J Magn Reson Imaging 37, 576–599.

Stoeck, C.T., Manka, R., Boesiger, P., Kozerke, S., 2012. Undersampled cine 3D tagging for rapid assessment of cardiac motion. J Cardiovasc Magn Reson 14, 60.

Swoboda, P.P., Larghat, A., Zaman, A., Fairbairn, T.A., Motwani, M., Greenwood, J.P., Plein, S., 2014. Reproducibility of myocardial strain and left ventricular twist measured using complementary spatial modulation of magnetization. J Magn Reson Imaging 39, 887–894.

Tobon-Gomez, C., De Craene, M., McLeod, K., Tautz, L., Shi, W., Hennemuth, A., Prakosa, A., Wang, H., Carr-White, G., Kapetanakis, S., Lutz, A., Rasche, V., Schaeffter, T., Butakoff, C., Friman, O., Mansi, T., Sermesant, M., Zhuang, X., Ourselin, S., Peitgen, H.O., Pennec, X., Razavi, R., Rueckert, D., Frangi, A., Rhode, K., 2013. Benchmarking framework for myocardial tracking and deformation algorithms: An open access database. Med Image Anal 17, 632–648.